Nuclear Inst. and Methods in Physics Research, A 875 (2017) 65–79

Contents lists available at ScienceDirect

Nuclear Inst. and Methods in Physics Research, A

journal homepage: www.elsevier.com/locate/nima

Commissioning of the Active-Target Time Projection Chamber

J. Bradt [a,b,*], D. Bazin [a,b,*], F. Abu-Nimeh [a,1], T. Ahn [c], Y. Ayyad [a,2], S. Beceiro Novo [a,b], L. Carpenter [a,b], M. Cortesi [a], M.P. Kuchera [a,3], W.G. Lynch [a,b], W. Mittig [a,b], S. Rost [a,b], N. Watwood [a,b], J. Yurkon [a]

[a] National Superconducting Cyclotron Laboratory, Michigan State University, East Lansing, MI 48824, USA
[b] Department of Physics and Astronomy, Michigan State University, East Lansing, MI 48824, USA
[c] Department of Physics, University of Notre Dame, Notre Dame, IN 46556, USA

ARTICLE INFO

Keywords:
Time projection chamber
Active target
Micromegas
Digital electronics

ABSTRACT

The Active-Target Time Projection Chamber (AT-TPC) was recently built and commissioned at the National Superconducting Cyclotron Laboratory at Michigan State University. This gas-filled detector uses an active-target design where the gas acts as both the tracking medium and the reaction target. Operating inside a 2T solenoidal magnetic field, the AT-TPC records charged particle tracks that can be reconstructed to very good energy and angular resolutions. The near-4π solid angle coverage and thick target of the detector are well-suited to experiments with low secondary beam intensities. In this paper, the design and instrumentation of the AT-TPC are described along with the methods used to analyze the data it produces. A simulation of the detector's performance and some results from its commissioning with a radioactive ^{46}Ar beam are also presented.

1. Introduction

Experiments using low-energy beams of radioactive ions from accelerators such as the recently completed ReA3 linac at the National Superconducting Cyclotron Laboratory (NSCL) at Michigan State University [1] present a special set of challenges. The usually low intensity of these beams requires a detector with a very high efficiency, while the low beam energies of 0.3 MeV/u to 6.0 MeV/u preclude the use of a thick solid or liquid target. One detector type particularly well suited to these experiments is a time projection chamber (TPC) used in an active target configuration. The main innovation of the active target design over a traditional TPC is that the detector gas also serves as the reaction target [2]. Since a reaction can occur anywhere within the detector's active volume, these reactions can be measured over a continuous, broad range of energies as the beam slows down within the gas volume. Because the reaction products emerge from within the tracking medium itself, very low energies can be measured, and the vertex of the reaction can be determined on an event-by-event basis. This method allows detection of reactions at low energy with a solid angle coverage close to 4π and without compromising the target thickness, as opposed to a passive target where the thickness has to be reduced enough for the reaction products to escape. In addition, excitation functions of cross sections can be measured with a single beam energy since the vertex energy can be reconstructed for each reaction.

To take advantage of this technique, the Active-Target Time Projection Chamber (AT-TPC) was recently constructed and commissioned at the NSCL. The AT-TPC is a full-scale version of the Prototype AT-TPC [3], a half-scale model that has already been successfully used in a number of experiments [4–6]. Since the design of the full-scale AT-TPC is quite similar to that of the Prototype AT-TPC, which has previously been described in detail [3], this article provides only a brief description of the detector that mainly serves to highlight the improvements made upon the prototype design (Section 2). Instead, the majority of this article is devoted to a description of the data analysis techniques (Section 3) and simulations (Section 4) developed for the AT-TPC in addition to some results from the detector's radioactive beam commissioning experiment (Section 5), which measured resonant proton scattering on ^{46}Ar.

* Corresponding authors at: National Superconducting Cyclotron Laboratory, Michigan State University, East Lansing, MI 48824, USA.
E-mail addresses: bradt@nscl.msu.edu (J. Bradt), bazin@nscl.msu.edu (D. Bazin).
[1] Present address: Molecular Biophysics and Integrated Bioimaging Division, Lawrence Berkeley National Laboratory, Berkeley, CA 94720, USA.
[2] Present address: Nuclear Science Division, Lawrence Berkeley National Laboratory, Berkeley, CA 94720, USA.
[3] Present address: Department of Physics, Davidson College, Davidson, NC 28035, USA.

http://dx.doi.org/10.1016/j.nima.2017.09.013
Received 10 March 2017; Received in revised form 1 September 2017; Accepted 5 September 2017
Available online 8 September 2017
0168-9002/

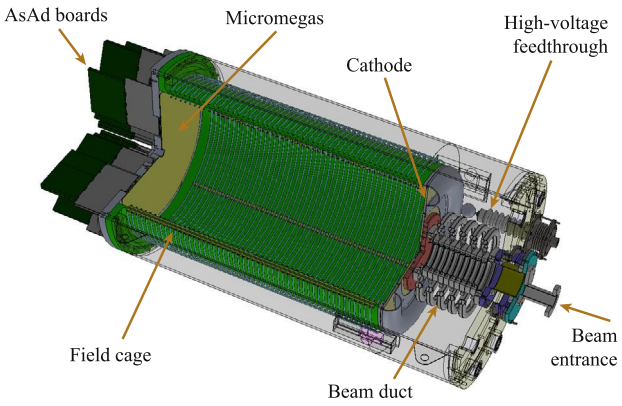

Fig. 1. A schematic view of the AT-TPC. The outer shielding volume was made transparent in this image to make the details of the inner volume more visible. Beam enters the detector through the beam duct at the right-hand side of the image and moves toward the sensor plane on the left. Some components of the digital electronics are shown mounted on the downstream end of the detector (see Section 2.4).

2. Detector design

As stated above, the design of the AT-TPC is similar to that of the half-scale Prototype AT-TPC [3]. The most important differences between the two detectors are the larger size of the full-scale AT-TPC, the improved sensor plane design, and the addition of a magnetic field. These improvements are discussed below along with a general description of the AT-TPC.

2.1. Overview

The AT-TPC consists of a cylindrical active volume of length 1 m and radius 29.2 cm surrounded by a larger concentric shielding volume (Fig. 1). The active inner volume is filled with a gas that provides scattering targets for the reaction and a tracking medium for the charged particles. The choice of fill gas depends on the experiment since it must contain the target nucleus of interest, but the detector has been successfully tested both with pure gases (including hydrogen, helium, isobutane, and carbon dioxide [7]) and with gas mixtures (including He + CO_2). The gas pressure is adjusted based on the incoming beam energy and the gas properties to give the desired particle range in the detector; it may be set to any value up to atmospheric pressure. The outer shielding volume is filled with an insulating gas such as nitrogen.

The dimensions of the detector were determined by the available space inside the large-bore solenoidal magnet in which it is installed. This magnet, which is capable of producing a field of up to 2 T at the center of its bore, was designed for a medical magnetic resonance imaging (MRI) machine and was moved to the NSCL from TRIUMF after being used for the TWIST experiment [8]. The AT-TPC is mounted coaxially on rails in the center of the magnet. The longitudinal magnetic field bends the trajectories of the emitted charged particles in order to determine their energies and aid in particle identification. Another direct benefit is the ability to track particles over longer paths, and for those that stop in the gas volume, to measure their total range. This ability is enhanced by the larger size of the full-scale AT-TPC as compared to the half-scale prototype.

The uniformity of the magnetic field is assured by the AT-TPC's central location in the solenoid, far from the fringe field regions. A calculated map of the axial component of the magnetic field inside the magnet is shown in Fig. 2. The total variation of the field inside the active volume of the AT-TPC, as indicated by the white rectangle, is only 20.42 mT, a fluctuation of 1.1 % compared to the value of 1.908 T at the center.

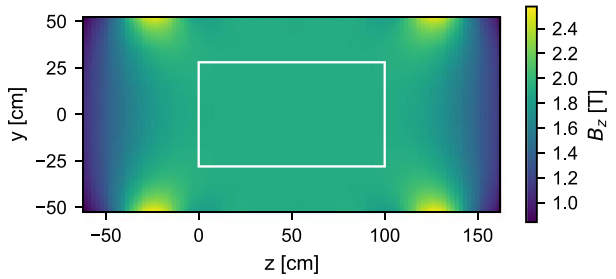

Fig. 2. Calculated map of the axial (z) component of the magnetic field within the bore of the solenoid. The center of the sensor plane is located at the origin. The boundary of the active volume is indicated with a white rectangle.

A uniform electric field is produced inside the active volume by applying a potential difference on the order of 10^4 V between the cathode located at the upstream end of the cylindrical volume and the anode at its downstream end. To ensure that the electric field is uniform, the wall of the active volume is surrounded inside and out by a field cage consisting of 50 concentric ring-shaped electrodes spaced 19.05 mm apart. The inner rings have a radius of 28.1 cm, while the outer rings have a radius of 31.1 cm. The rings are connected to each other and to the anode and cathode by a chain of 20 MΩ resistors that gradually steps down the voltage between each ring, establishing evenly spaced equipotentials for the electric field. An additional voltage on the order of 500 V is applied to the ring closest to the sensor plane to account for the distance that the sensor plane projects out from the downstream end plate.

To check the uniformity of the electric field, an electric field calculation was performed[4] using Garfield [9]. As discussed by Suzuki et al. [3], Garfield is limited to two-dimensional geometries, so the electric field cage was approximated in two dimensions using a collection of infinite wires. The result of the calculation is shown in Fig. 3, where the uniformity of the field in the drift region is apparent. This conclusion is supported by the lack of visible distortions in recorded tracks, even when particles travel near the edges of the active volume. Finally, the region closest to the rings, which will have the least-uniform electric field, is not seen by the sensor plane since the sensor plane's diameter is 1.2 cm smaller than the diameter of the inner field cage rings.

The beam enters the active volume through a 3.6 μm thick, 25.4 mm diameter aluminized para-aramid window at the cathode end of the detector and travels through the gas, ionizing it. The ionization electrons are transported by the electric field from where they are produced to the anode end of the detector, which is composed of a sensor plane equipped with a bulk-fabricated [10] Micromegas device [11]. The signals from the sensor plane are then read out by digital electronics mounted on the outside of the flange enclosing the active volume. These front-end electronics boards are connected to the sensor plane via feedthrough boards that isolate them from the gas volume. The absence of cables between the sensor plane and the front-end preamplifiers simplifies the assembly of the electronics and greatly reduces the noise. This is discussed further in Section 2.4.

2.2. Sensor plane

The sensor plane consists of a circular printed circuit board of radius 27.5 cm covered with 10 240 gold-plated triangular electrodes, or *pads*. The pads are arranged in a hexagonal inner region of 6144 small pads with height 0.5 cm surrounded by an outer region of 4096 large pads with height 1.0 cm (Fig. 4). The inner region of half-scale pads provides a finer resolution near the reaction vertex, which will generally occur near the central axis of the detector. Larger pads are used instead in the outer region to help keep the total number of channels reasonable.

[4] F. Montes, private communication.

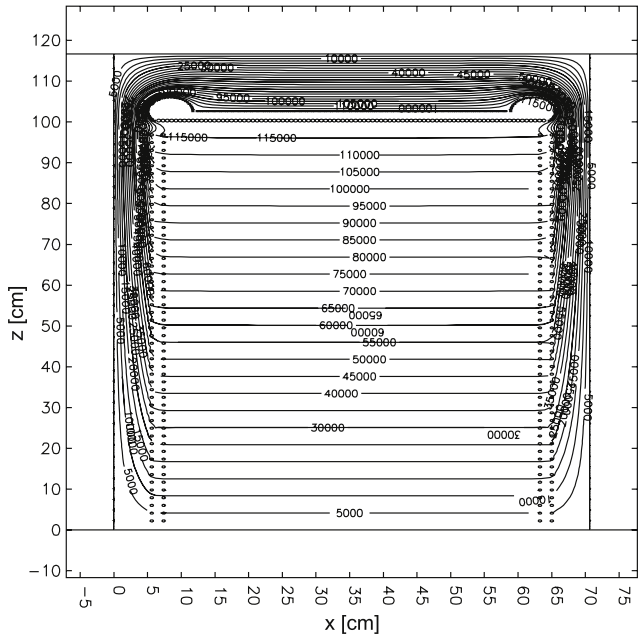

Fig. 3. Equipotentials of the electric field in a cross section of the AT-TPC as calculated by Garfield. The cathode is at the top of the figure, shown with the corona ring that prevents discharges between it and the wall of the outer volume. The rings appear as small circles along the left and right sides of the figure.

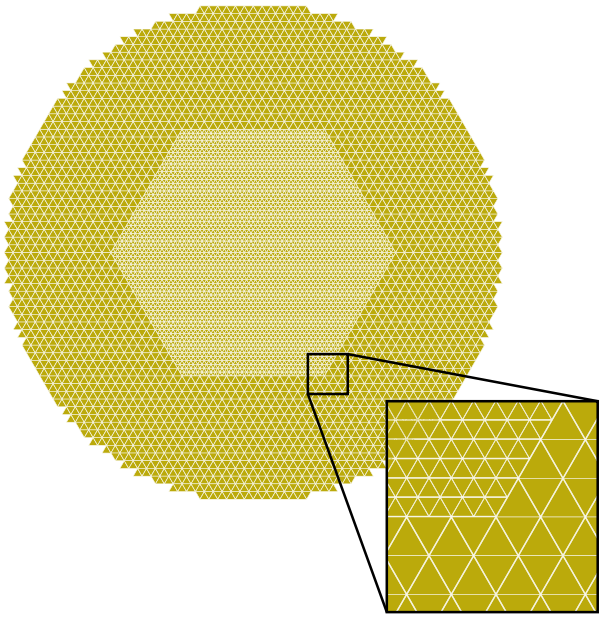

Fig. 4. Layout of the pad plane. The inset shows a closer view of one corner of the hexagonal inner region.

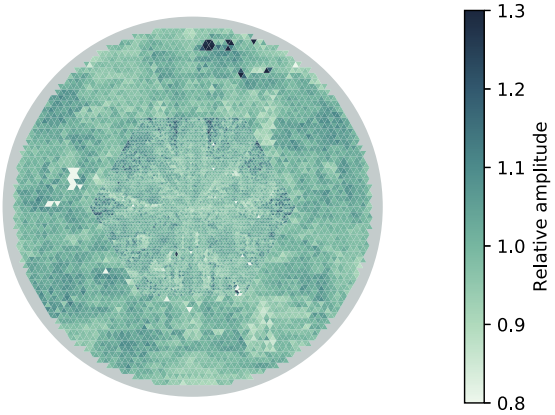

Fig. 5. Relative pulser signal amplitude across the sensor plane.

The triangular pad shape was chosen to maximize the spatial resolution of the detector. When a charged particle track crosses a series of adjacent triangular pads, the amount of charge deposited on each pad is staggered. This staggering pattern changes significantly with even a small change in the orientation of a track, allowing a greater sensitivity and better angular resolution.

This pad plane design provides a vast improvement in spatial and angular resolution when compared to the design used in the Prototype AT-TPC. That device uses a sensor plane with 253 pads laid out as a set of segmented rings (see [3, Fig. 5]). While that design allows binary events to be reconstructed to a reasonable precision in the smaller volume of the Prototype AT-TPC, the 10 240 pads of the full-scale sensor plane permit a true three-dimensional event reconstruction for arbitrary reactions. Additionally, the design of the full-scale AT-TPC allows for the possibility of eventually constructing a modified pad plane with a hole in the center. Recoil nuclei could then pass through this hole and out of the detector through a flange in the downstream end plate. The AT-TPC could then be used in conjunction with device such as the S800 Spectrograph at the NSCL to identify the recoil nuclei.

The Micromegas device installed on the sensor plane consists of a micromesh supported by insulating pillars at 122 μm above the pads.[5] A potential on the order of 100 V to 1000 V is applied between the mesh and the pad plane to produce a region of high electric field just above the pads. When ionization electrons drift into this region, they are multiplied via an avalanche process and produce a detectable signal on the pad located directly underneath the avalanche. Since the distance between the pad plane and the mesh is very small compared to the size of the pads, the signal induced by a given ionization electron is usually confined to one pad only.

The gain of the Micromegas depends strongly on the size of the gap between the pads and the mesh. This gap should be very uniform thanks to the bulk fabrication process used to install the mesh on the sensor plane [10]. The uniformity was tested by applying a 3 V pulser signal to the mesh and recording the signals induced on the pads. The amplitude of the signal induced by the pulser on a given pad depends on the capacitance between the mesh and the pad, which is inversely proportional to the local mesh gap. The amplitude also depends on the preamplifier gain in each channel, which was set to 120 fC. The signal amplitudes were normally distributed with mean 457 bins and standard deviation 32 bins for the small pads and mean 1547 bins and standard deviation 143 bins for the large pads. The gain is larger for the large pads since it is proportional to pad area, so the signal amplitude in each channel was then renormalized to 1 by dividing the amplitudes from each group of pads (large and small) by the mean amplitude within that group. The resulting normalized amplitudes are shown on the sensor plane in Fig. 5. Aside from a few malfunctioning channels, the signal amplitude is quite uniform across the sensor plane, and more importantly, the variations that do appear are generally randomly distributed aside from a faint asterisk-like pattern that coincides with boundaries of different readout electronics cards. This indicates that the variations in amplitude are more likely due to natural variations in gain between channels in the electronics than due to variations in the mesh gap.

[5] S. Aune, private communication.

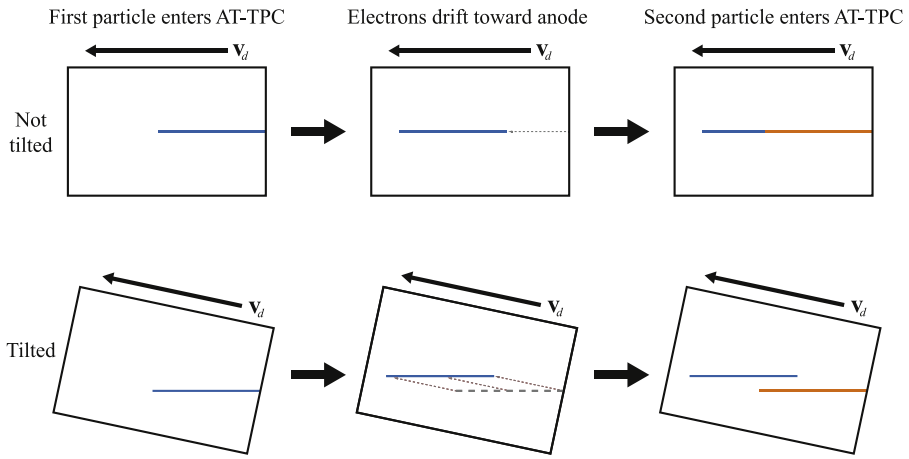

(a) Principle of pileup separation.

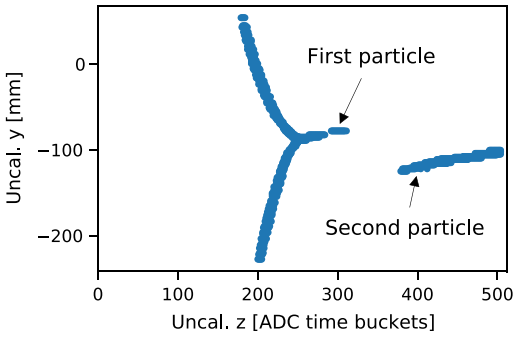

(b) Example event.

Fig. 6. Illustration of pileup separation using the tilt angle. (a) In the standard configuration (top), a particle enters the AT-TPC, and the ionization electrons drift along the beam axis. When a second track enters the detector, it is collinear with the first track. In the tilted configuration (bottom), the electrons freed by the first particle drift in a direction that is not parallel to the beam axis. The second track is then separated from the first. (b) An example α-α scattering event with pileup. The second beam particle is not collinear with the first due to the detector tilt.

The gains found by this method can also be used to calibrate the recorded signals to a uniform gain, but this was not done in the analysis presented below since the effect is quite small.

2.3. Tilting the detector

The AT-TPC is normally coaxially centered within the bore of the magnet, but the detector's support carriage is equipped with a small jack that allows the detector to be optionally tilted by 6.2° with respect to the central axis of the solenoid. Tilting the detector can be advantageous for two reasons. First, the tilt angle projects the beam track onto more pads than the few located at the center of the pad plane, thereby increasing the detector's sensitivity for small scattering angles. Second, it allows a better separation of the pileup tracks that occur when several beam particles enter the chamber during a single event since their tracks will no longer be collinear (see Fig. 6(a)). Due to these advantages, the detector was used in the tilted configuration for the simulations in Section 4 and the commissioning experiment in Section 5.

The detector tilt does, however, complicate track reconstruction since in the tilted configuration, the electric and magnetic fields are no longer aligned. This means that the ionization electrons no longer drift parallel to the beam axis, but are instead deflected by some amount in the x and y directions as defined in Fig. 7. This will be discussed in Section 3.1 below.

2.4. Electronics

The AT-TPC is instrumented with digital electronics developed by the Generic Electronics for TPCs (GET) collaboration [12]. This equipment

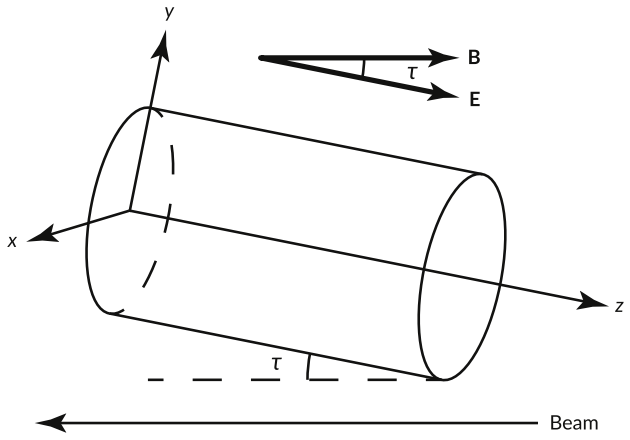

Fig. 7. The coordinate system used in the analysis. The x and y directions are defined by the geometry of the sensor plane. The z direction points upstream, placing the sensor plane at $z = 0$. The detector tilt angle τ is also the angle between the electric and magnetic field vectors since the solenoid is aligned with the beam axis. It should be noted that this system is left-handed.

provides a fully digital data acquisition system that is capable of digitizing and recording the full trace for each of the 10 240 channels in the detector.

The electronics hardware is divided into a hierarchy of several modules (Fig. 8). At the lowest level of the hierarchy is the AGET chip, a custom ASIC that controls the sampling and shaping of the

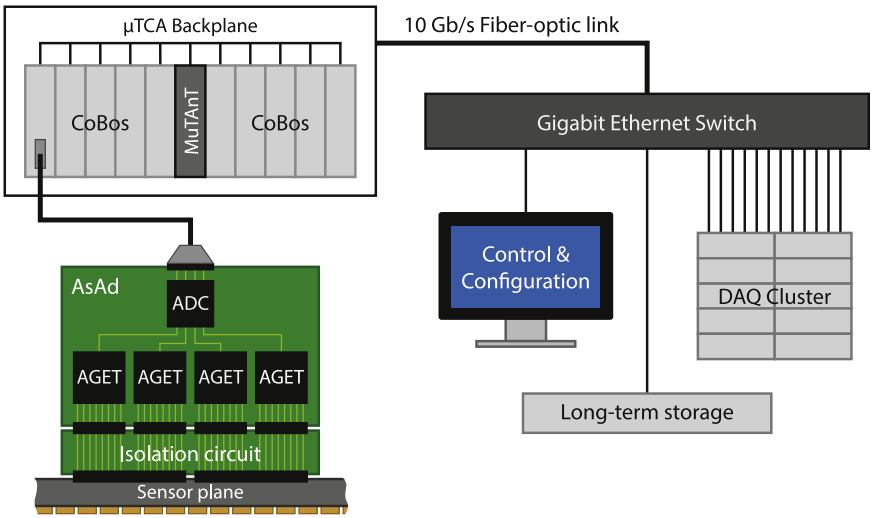

Fig. 8. Schematic view of the GET electronics system. For clarity, only one AsAd is shown, but in reality, 40 AsAds are used to instrument the AT-TPC.

signals and compares the signals to a threshold to generate a channel-level trigger. The AGET amplifies the incoming signal with a variable-gain charge-sensitive preamplifier and performs pole-zero correction. It then stores samples of the analog signal in a switched capacitor array (SCA) which acts as a circular buffer [13,14]. Each AGET can read out 64 channels from the detector in addition to four fixed-pattern noise channels. The fixed-pattern noise channels are structurally identical to the physics channels, but without inputs [13,14]. This allows the data to be corrected for low-frequency electronic noise.

The AGETs are mounted in groups of four on AsAd (**A**SIC **S**upport and **A**nalog to **D**igital conversion) boards. In addition to the four AGETs, each AsAd board houses a four-channel, 12-bit ADC. When a trigger is issued, the ADC digitizes the sample outputs from each AGET chip and transmits them via a serial link [14]. Between triggers, the ADC digitizes and transmits the multiplicity signal from each AGET integrated over an adjustable-width sliding time window.

The input end of each AsAd board is attached to an isolation circuit that prevents sparks in the detector from damaging the electronics, and this assembly is then mounted on the downstream end of the AT-TPC as shown in Fig. 9 and connected directly to the sensor plane. This design was chosen to minimize the distance that analog signals must travel before being digitized, reducing the capacitance and potential noise in the data. The mean noise level across the system was quantified at 972 electrons by taking the standard deviation of the baseline signal from each channel using a gain of 120 fC. The noise level in each channel is plotted as a function of printed circuit board (PCB) trace length in Fig. 10. These traces link the pads to connectors on the back of the sensor plane that couple to the AsAd assemblies, and the traces vary in length due to the complex routing pattern required to connect 10 240 pads to 40 connectors. Fig. 10 shows that longer trace lengths are generally correlated with higher noise levels, but this dependence is not especially strong.

While it provides a low baseline noise level, the direct connection between the front-end electronics and the sensor plane also means that the AsAd assemblies operate inside the high magnetic field of the solenoid during experiments. However, this application was accounted for in the design of the GET electronics system, and tests have shown that the performance of the system is the same with and without the magnetic field.

The top level of the GET electronics hierarchy is the CoBo (**Co**ncentration **Bo**ard). Each of the AT-TPC's 10 CoBos is connected to four AsAd boards. When a trigger is issued, the CoBo collects the data from these boards, applies an event time stamp, and builds the event [14]. It then sends the event over a 10 Gb/s fiber-optic link to a network switch to be distributed to a cluster of computers for storage.

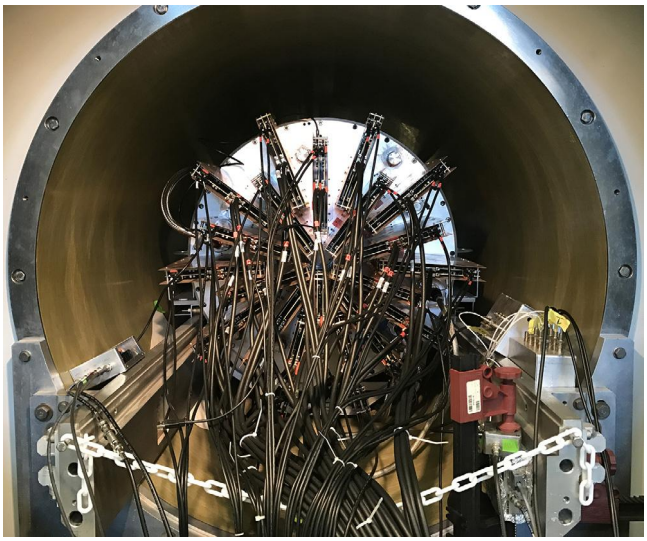

Fig. 9. A photograph of the fully instrumented AT-TPC mounted inside its solenoid magnet. The 40 AsAds are mounted directly on the downstream end flange in groups of two, surrounded by copper shielding.

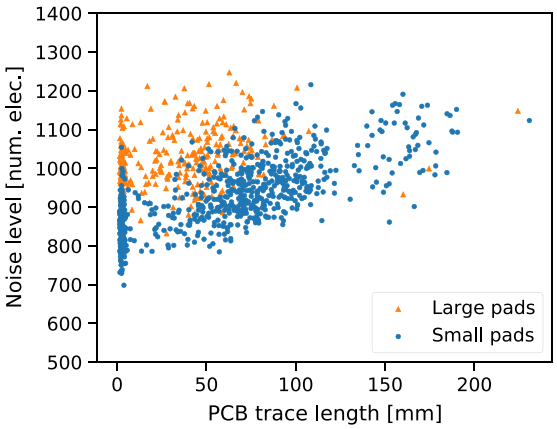

Fig. 10. Noise level in each channel as a function of the length of the PCB trace linking each pad to the front-end electronics. Longer traces and larger pads tend to be associated with more noise.

To keep the CoBos synchronized, an additional board called the MuTAnT (**Mu**ltiplicity, **T**rigger, **An**d **T**ime) distributes a global time stamp and manages clock synchronization across the system [14]. The MuTAnT board is designed to collect all of the running multiplicities and hit patterns from the CoBos and combine them in various ways to generate a global trigger. The most straightforward method consists of simply summing the multiplicities to generate a trigger when a global threshold is reached. This is referred to as a Level 1 trigger. Other more complex trigger decisions can be used that involve matching a predefined pattern of hit channels (a Level 2 trigger). In the data and tests presented in this article, the MuTAnT board was not yet available due to its delivery schedule; therefore, the trigger was performed externally as a logical OR of each CoBo's multiplicity (see Section 2.7).

2.5. Data acquisition

The AT-TPC is read out by a custom distributed, digital data acquisition system. As described previously, the ten CoBos are connected via a high-speed network to a cluster of ten commodity desktop computers. Each of these computers runs a data router program developed by the GET collaboration to record the data from one CoBo. Distributing the data over ten computers greatly increases the throughput of the system, which is important for a detector that can produce up to 11 MB of raw data per event in full-readout mode.

The system is controlled by the Electronics Control Core (ECC) server, which was also developed by the GET collaboration. This software reads configuration parameters for the CoBos and MuTAnT from an XML file and uses this information to set the appropriate registers on the boards and establish communications between the boards and the data routers. The ECC server is also responsible for starting and stopping data taking on the CoBos.

To make this complex system easier to control for experimenters, a web-based graphical user interface was developed at the NSCL. It presents an interface that allows the user to choose which electronics configuration files to use, configure the electronics, start and stop runs, and monitor the system. The web application format was chosen since it allows easy remote access to the data acquisition computers, which must sit close to the AT-TPC in the experimental area. This interface communicates with the ECC servers through standard web protocols.

2.6. Ion chamber

A small, cylindrical ion chamber was constructed and inserted into the beam line just upstream of the AT-TPC. The chamber is 5 cm long and contains 5 thin foils mounted at equal intervals along the axial direction. The foils are 25.4 mm in diameter and consist of approximately 400 $\mu g\,cm^{-2}$ of aluminum evaporated on a plastic substrate. The outermost two foils are grounded and serve as entrance and exit windows, while the inner three foils establish equipotentials for the electric field. The drift direction is parallel to the beam, and signals are read out from the center foil, which is kept at high voltage.

This ion chamber serves two purposes. First, the energy loss data from the ion chamber can be used to help separate the desired beam particles from contaminants. In the commissioning experiment, the resolution of the ion chamber was sufficient to separate the ^{46}Ar nuclei of interest from the ^{46}K contaminant arising from β-decay (see Fig. 11). Second, the timing signal from the ion chamber is used to prevent the AT-TPC from triggering on events that are not correlated with a beam particle and to establish an absolute, global time reference for each event that corresponds to when the beam particle entered the active gas volume. The data from the ion chamber is digitized using a 12-bit flash ADC VME module and recorded using a separate DAQ from the main system. The two DAQ systems were synchronized using a common sequential event ID during the commissioning experiment presented below, but in the future, the systems will be synchronized using a common timestamp output by the MuTAnT board.

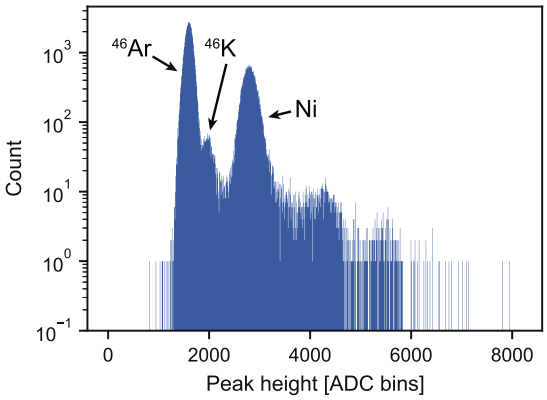

Fig. 11. Ion chamber spectrum of a subset of events from the commissioning experiment. The ion chamber was able to separate the ^{46}Ar nuclei from their ^{46}K daughters and a nickel contaminant.

2.7. Trigger

When not using a MuTAnT board, the GET electronics can be triggered externally by a signal based on the number of hit pads in the detector and a beam trigger. Each AGET outputs a multiplicity signal which is derived from the number of channels in that AGET that are above some pre-set threshold amplitude [14]. The multiplicities from each AGET are collected by their controlling CoBos to produce a CoBo-level multiplicity signal. The CoBos then compare their summed multiplicity signals to a CoBo-level multiplicity threshold and output a trigger signal if the summed multiplicity is above threshold. These trigger signals are then collected from the 10 CoBos and combined using a logical OR operation.

In addition to the multiplicity signals, a trigger signal is derived from the ion chamber output. This ion chamber trigger is then delayed and compared to a coincidence window which was opened by the CoBo multiplicity trigger. If the delayed ion chamber signal falls within this coincidence window, a trigger signal will be generated and distributed to the 10 CoBos at that time. The trigger is based on the delayed ion chamber signal to ensure that the trigger timing is always constant with respect to the arrival of the beam particle into the AT-TPC, rather than the delayed time of arrival of the drifting electrons. The latter is highly dependent on the trajectory of the charged particle emitted during the reaction, and therefore it does not provide a good timing reference. This reference is essential to establish the relationship between the measured time of the signals and the position along the drift direction of the electrons. This relationship is then used to deduce the absolute position of the tracks in this direction.

2.8. Pad configuration

The GET digital electronics system allows the readout and trigger attributes of each channel to be set individually. In particular, when configuring the electronics, one can choose whether each channel should be read always or read only when it registers a hit. Additionally, the contribution to the global hit multiplicity can be enabled or disabled on a channel-by-channel basis, and the threshold and preamplifier gain for each channel can be set independently. These features are essential in the low-energy domain covered by the AT-TPC where both the beam particles and reaction products may be stopped in the detector, and an internal trigger must be generated to select only events in which a reaction occurred.

A graphical configuration tool has been created to set these readout and trigger attributes for each pad and write them into the configuration file that is used to program the electronics. The pad region corresponding to the incoming beam track can then be excluded from the trigger,

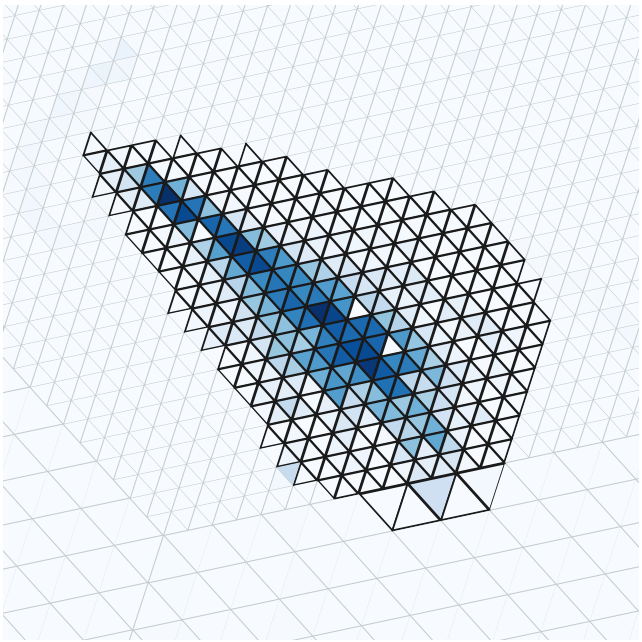

Fig. 12. An example trigger exclusion region used for ^{4}He + ^{4}He scattering. 100 accumulated beam-like events are shown in shades of blue, where darker colors indicate that more charge was deposited in that pad. The pads outlined in black were excluded from the trigger. The shape of this region is the result of the detector's tilt with respect to the magnetic field, as described in Section 2.3. (For interpretation of the references to color in this figure legend, the reader is referred to the web version of this article.)

as shown in Fig. 12 for the case of ^{4}He + ^{4}He scattering. The gain of the electronics is also tunable at the channel level and can be used to eliminate or mitigate saturation effects in regions where the density of ionized electrons is much higher due to a larger energy loss, as is the case in the ^{46}Ar(p, p) example described in later sections.

2.9. Efficiency considerations

As stated previously, the AT-TPC has a very high theoretical efficiency with respect to the angular distribution and energy of the outgoing reaction products. In practice, however, the efficiency of the detector is limited by several factors. The most significant limitation comes from pileup events where multiple beam particles enter the active volume during the time window of a single event. Although these can in principle be identified and separated when the detector is tilted (as discussed in Section 2.3), this was not possible during the commissioning experiment since the beam tracks could not be reconstructed reliably. Therefore, any pileup events had to be discarded. For the commissioning experiment, 61 % of the dataset consisted of single-particle events, although this value depends entirely on the properties of the beam.

A secondary limitation on the efficiency is the dead time of the electronics. Any triggers that arrive while the GET system is busy recording an event are rejected, leading to missed events. The GET electronics were live 78 % of the time during the commissioning experiment, where the average event rate was approximately 10 Hz.

A final limitation on the efficiency is imposed by the choice of trigger exclusion regions as discussed in Section 2.8 above. The effects of these regions on the efficiency can be understood through simulations. These simulations were performed for the trigger regions used in the commissioning experiment, and the results are described in Section 4.3 below.

3. Data analysis

Extracting physics results from the data recorded by the AT-TPC requires a multi-step analysis process. This process involves reconstructing three-dimensional tracks from the electronics signals, cleaning the tracks to remove noise and pileup, and fitting the tracks using a Monte Carlo algorithm. An overview of the analysis process will be presented in this section.

3.1. Track reconstruction

The first step of the analysis is to reconstruct three-dimensional tracks from the recorded signals. The time-domain signals are converted to a set of discrete points (x_i, y_i, z_i) with associated peak amplitudes a_i. Given the high granularity of the pad plane and the low occupancy of the events of interest (only a few tracks are expected per event), it is reasonable to assume that each pad is activated only once in a particular event. The (x, y) coordinates for a particular channel are then the centroid of the corresponding triangular pad, and the uncalibrated z position is the time corresponding to the center of gravity of the largest pulse recorded by the digital electronics. The amplitude of the signal is calculated by comparing the maximum of the found peak with the baseline signal just before it.

The reconstructed data must then be transformed to change the z coordinate into a distance unit. If the detector is not tilted, or the magnetic field is not on, then the ionization electrons drift along the electric field lines and the transformation is simply given by

$$z = \frac{v_d T}{f} \tag{1}$$

where v_d is the constant electron drift velocity in the detector, T is the time bucket index (which corresponds to the uncalibrated z position), and f is the clock frequency of the electronics.

If the detector is tilted with a nonzero magnetic field, on the other hand, the transformation is more complex. In this case, a vectorial drift velocity must be used to compensate for the additional drift in the x and y directions. This drift velocity vector can be derived from the Langevin equation that describes the motion of an electron with mass m and charge e in the detector gas [15]:

$$m\frac{d\mathbf{v}}{dt} = e(\mathbf{E} + \mathbf{v}\times\mathbf{B}) - \frac{m}{\tau}\mathbf{v}. \tag{2}$$

Here, $\mathbf{E}$ and $\mathbf{B}$ are the electric and magnetic field vectors, $\mathbf{v}$ is the electron's velocity, and τ is the mean time between collisions. This differential equation has a steady-state solution [15]

$$\mathbf{v}_D = \frac{\mu E}{1+\omega^2\tau^2}\left[\hat{\mathbf{E}} + \omega\tau\left(\hat{\mathbf{E}}\times\hat{\mathbf{B}}\right) + \omega^2\tau^2\left(\hat{\mathbf{E}}\cdot\hat{\mathbf{B}}\right)\hat{\mathbf{B}}\right]. \tag{3}$$

Here, $\mathbf{v}_D$ is the drift velocity vector, $\omega = eB/m$ is the cyclotron frequency, $\tau = mv_D/eE$ is the mean time between collisions, and $\mu = e\tau/m$ is the electron mobility in the gas [15]. These values can be combined to show that $\mu E = v_D$ and $\omega\tau = (B/E)v_D$, so Eq. (3) can be rewritten as

$$\mathbf{v}_D = \frac{v_D}{1+\left(\frac{B}{E}v_D\right)^2}\left[\hat{\mathbf{E}} + \frac{B}{E}v_D\left(\hat{\mathbf{E}}\times\hat{\mathbf{B}}\right) + \left(\frac{B}{E}v_D\right)^2\left(\hat{\mathbf{E}}\cdot\hat{\mathbf{B}}\right)\hat{\mathbf{B}}\right]. \tag{4}$$

The values of the electric and magnetic field magnitudes E and B are then measured experimentally, and the drift velocity magnitude v_D can be found empirically or from a calculation or a table. In the coordinate system shown in Fig. 7, the electric field is $\mathbf{E} = E\hat{z}$ and the magnetic field is $\mathbf{B} = B\left[\sin(\theta_t)\hat{y} + \cos(\theta_t)\hat{z}\right]$ for a tilt angle θ_t, so Eq. (4) can be

simplified to yield the following components:

$$v_x = \frac{v_D}{1+\left(\frac{B}{E}v_D\right)^2}\left(\frac{B}{E}v_D\right)\sin\theta_t \tag{5}$$

$$v_y = \frac{v_D}{1+\left(\frac{B}{E}v_D\right)^2}\left(\frac{B}{E}v_D\right)^2\sin\theta_t\cos\theta_t \tag{6}$$

$$v_z = \frac{v_D}{1+\left(\frac{B}{E}v_D\right)^2}\left[1+\left(\frac{B}{E}v_D\right)^2\cos^2\theta_t\right]. \tag{7}$$

These components of the drift velocity vector can then be used to transform the raw, uncalibrated data recorded by the digital electronics into a calibrated coordinate system where all three coordinates are spatial and the tilt angle has been accounted for. The following relations are used for this calibration:

$$x = x_0 - \frac{v_x T}{f} \tag{8}$$

$$y = y_0 - \frac{v_y T}{f} \tag{9}$$

$$z = \frac{v_z T}{f}. \tag{10}$$

Here, T is the ADC time bucket, f is the clock frequency of the electronics, and (x_0, y_0) is the position as projected onto the pad plane. This transformation assumes that the location of the sensor plane corresponds to time $T = 0$, so any offset caused by a delay in the electronics must be subtracted from T before transforming the data.

3.2. Noise removal

The reconstructed tracks generally contain some noise points and structures that need to be removed before fitting. There are generally two types of noise present in the events: uncorrelated, random points from channels that were triggered by electronic noise, and correlated structures of points created by cross-talk in the electronics. The uncorrelated points are easily removed by using a neighbor-counting algorithm to eliminate points that have too few neighbors inside a small radius. The correlated noise is removed using a procedure [16,17] based on the Hough transform [18], a line recognition technique commonly used in image analysis and computer vision.

When processing the spiral-shaped tracks produced by the AT-TPC in a magnetic field, the center of curvature of the spiral is first found using a version of the Hough transform that is modified to find circular structures [19,20]. The center of curvature is used to "unwrap" the spiral into a series of parallel line segments in the space of track arc length vs. z. These line segments are identified using the ordinary Hough transform, and points that are not near an identified line segment are discarded as noise. This process is illustrated in Fig. 13, and it will be described in detail in a forthcoming publication [17].

3.3. Monte Carlo fit

After noise removal, the tracks are analyzed by using a Monte Carlo fitting method to find a complete set of parameters describing the state of the tracked particle at the beginning of the track. The particle state is parameterized in six dimensions using the location of the reaction vertex (x_0, y_0, z_0), the initial kinetic energy (E_0), and the two angles describing the orientation of the particle's initial velocity with respect to the beam axis (θ_0, ϕ_0). Fitting begins by generating a large ($N \approx 500$) set of possible sets of parameters from a uniform distribution. Each of these candidate tracks is then simulated by propagating the particles using the Lorentz force and the stopping power of the detector's fill gas as calculated by SRIM [21].

Instead of explicitly simulating interactions between drift electrons and the gas, the amount of primary ionization is estimated by dividing the energy lost by the tracked particle in each time step of the simulation by the ionization potential of the gas to produce a charge. Lateral diffusion of the drift electrons is modeled by dividing this charge between a central point and 8 outer points spread in a circle around the central point at 45° intervals. The radius of this circle is taken from the standard deviation of the electron diffusion distribution

$$\sigma = \sqrt{2Dt}, \tag{11}$$

where t is the total drift time, which is proportional to z, and D is a diffusion constant that is determined empirically. The central point of this simulated diffusion distribution is given 40 % of the total charge, and each of the 8 outer points is given 7.5 % of the total charge. These values were based on a two-dimensional normal distribution with standard deviation σ. Each of these points is then projected onto the pad plane using the drift velocity vector found by the process described in Section 2.3. As discussed in that section, propagating the charge along this drift velocity vector accounts for the lateral drift produced by the non-parallel electric and magnetic fields resulting from the detector tilt.

The response of the electronics to each of these diffused points is then simulated to produce a simulated signal for each pad. The signals are produced using the function

$$f(q,t) = \frac{G_\mu q}{G_{\text{elec.}} N_{\text{ADC}} C_{\text{norm}}}\left(\frac{t}{s}\right)^3 e^{-3(t/s)}\sin\left(\frac{t}{s}\right) \tag{12}$$

where G_μ is the Micromegas gain, q is the amount of charge deposited, $G_{\text{elec.}}$ is the gain of the GET electronics, $N_{\text{ADC}} = 4096$ is the number of ADC bins, t is time, s is the shaping time of the electronics, and $C_{\text{norm}} = 0.044$ is a normalization factor that rescales the time-dependent part of the function to have a maximum amplitude of 1. In the commissioning experiment, the shaping time was 280 ns, the electronics gain was 120 fC, and the Micromegas gain was taken to be 500.

The tracks are finally compared to the data using an objective function containing contributions from the track's position, its energy loss profile, and the location of its vertex. The position component of the objective function is a simple least-squares comparison between the track generated by the Monte Carlo algorithm and the track measured in the experiment. The generated track's x and y components are linearly interpolated as a function of z to give continuous functions $\tilde{x}(z)$ and $\tilde{y}(z)$. These functions are then evaluated at each of the measured track's z positions and compared to the measured x and y values. This gives the expression

$$\chi^2_{\text{pos}} = \frac{1}{N}\sum_{i=0}^{N}\frac{[\tilde{x}(z_i)-x_i]^2+[\tilde{y}(z_i)-y_i]^2}{\sigma^2_{\text{pos}}}, \tag{13}$$

where N is the number of data points in the measured track, and σ_{pos} is an expected deviation. This deviation was chosen to be 0.5 cm since that is approximately the amount of uncertainty introduced by taking the (x, y) position of each point to be the centroid of the corresponding pad.

The energy component of the objective function is produced by projecting each generated track onto the pad plane as discussed above and comparing the resulting hit pattern to the measured hit pattern. This gives a function of the form

$$\chi^2_{\text{en}} = \frac{1}{N_{\text{hit}}}\sum_{\text{hit pads}}\frac{\Delta A^2}{\sigma^2_{\text{en}}}. \tag{14}$$

Here A represents the total charge deposited in a particular pad. The normalization constant σ_{en} was chosen to be 10 % of the maximum value of A present in the measured track. This value was chosen based on the pulser measurements shown in Section 2.2 which demonstrated a variation of approximately 10 % in gain between channels. The sum is taken over all pads that were hit by the measured track, and N_{hit} is the number of such pads. Limiting the sum to pads present in the measured event helps the fit converge when parts of the track are missing since otherwise χ^2_{en} would have an unbalanced contribution from all the pads that are present in the generated track but not the measured one.

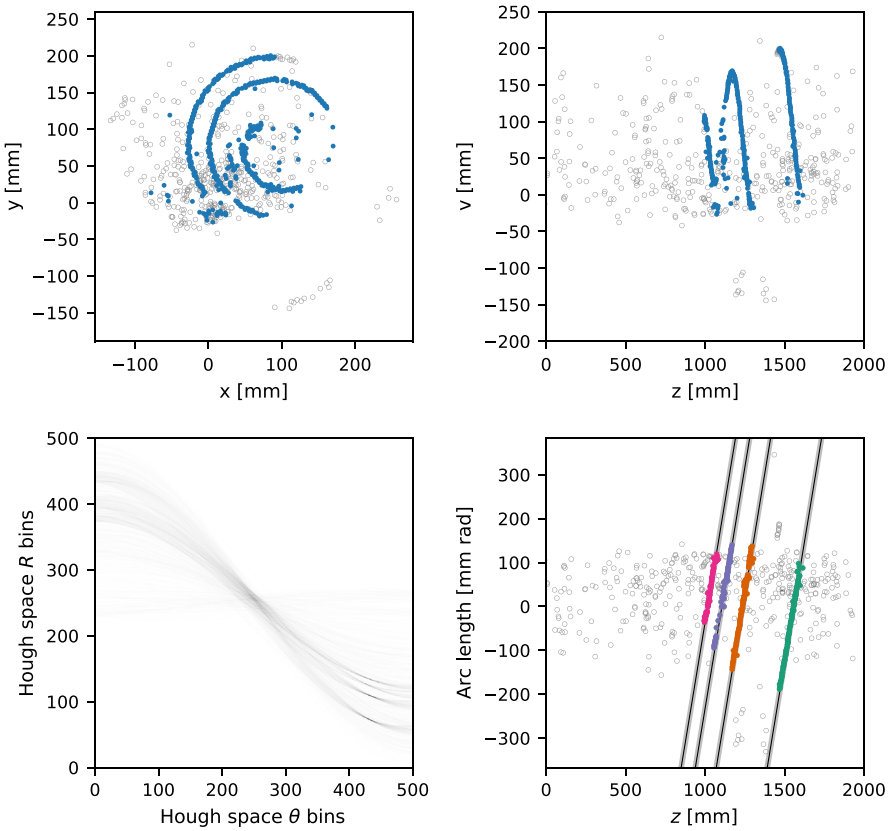

Fig. 13. Removing noise from an event using the Hough transform. The top two plots show two projections of an event after noise removal. Points that are identified as part of the track are shown with filled circles, while the noise points are marked with empty circles. The bottom left plot shows the Hough space calculated for the event; peaks in the Hough space correspond to lines in the data. The bottom right plot shows the four line segments identified in the arc length space.

The final component of the objective function helps constrain the reaction vertex to be near the beam track:

$$\chi^2_{\text{vert}} = \frac{(x_0 - x_{\text{beam}})^2 + (y_0 - y_{\text{beam}})^2}{\sigma^2_{\text{vert}}}. \tag{15}$$

This is a simple quadratic constraint on the (x, y) location of the vertex that imposes a penalty on the fit if the vertex is not near the beam. The parameter σ_{vert} can be tuned as needed to control the stringency of this restriction. A value of 7.1 mm was found to work well for this dataset. In experiments where the beam track is not visible, such as the ^{46}Ar(p, p) example shown below, the beam is assumed to lie along the z axis of the beam-centric coordinate system used in the analysis, so x_{beam} and y_{beam} are taken to be zero.

The complete objective function is, then, the sum of these three components:

$$\chi^2 = \chi^2_{\text{pos}} + \chi^2_{\text{en}} + \chi^2_{\text{vert}}. \tag{16}$$

Once all of the candidate tracks have been simulated and compared to the data, the one with the smallest value of the objective function is selected. The parameter space is then re-centered around this point and shrunk in each dimension by a fixed amount. This process is repeated several times until the results converge around the best-fit solution (see Fig. 14).

This simulation-based fitting technique is necessary because the tracks cannot be described by an analytic function. In low-energy experiments with the AT-TPC, the reaction products are typically stopped in the active volume of the detector so that the range of the particles can be measured. In a magnetic field, this produces helices with a radius of curvature that changes in accordance with the Bragg curve-shaped energy loss profile of the tracked particle in the gas. This is quite different from high-energy experiments where the proportion of the initial energy that is lost to the gas is negligible and the tracks can be described quite well as circular helices.

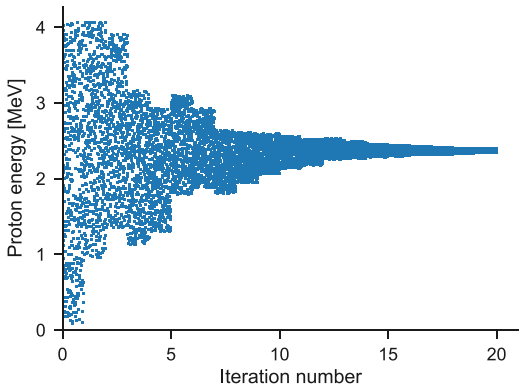

Fig. 14. Energy values sampled by the Monte Carlo algorithm while fitting one event. Each 500-sample iteration of the code is visible as a large-scale block in this plot. Similar plots can be made for each of the other fit parameters.

One limitation of this method is the large amount of computation required to simulate the 10^3 to 10^4 candidate tracks needed to fit each event. This was addressed by using multi-core processors to simulate the candidate tracks in parallel, reducing the runtime by up to an order of magnitude. Further improvements in runtime were achieved by analyzing each hour-long experimental run separately on a computer cluster, allowing many runs to be analyzed simultaneously.

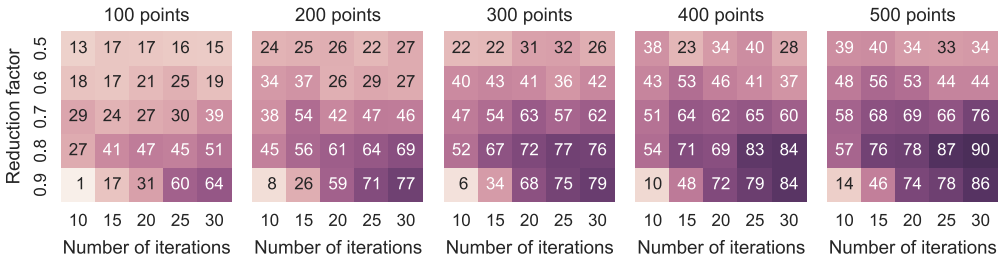

Fig. 15. Results of a convergence study for a simulated proton track that was fit using various sets of Monte Carlo parameters. Subplots represent different numbers of points T per iteration. Within each plot, rows represent the reduction factor R, and columns represent the number of iterations I. The number in each cell represents the percentage of the 1000 trials run for each set of parameters in which the optimizer converged to the correct minimum.

3.4. Checking convergence

The Monte Carlo algorithm described above does not include an explicit test for convergence, so the parameters of the fitter must be chosen in such a way that convergence is likely. There are three main parameters that control the convergence of the fit: the number of candidate tracks T generated per iteration, the number of iterations I, and the reduction factor R by which the parameter space is compressed after each iteration.

The values of T and R must be chosen carefully to prevent the fitter from converging to local minima. Much like in the process of simulated annealing, it is important to reduce the size of the parameter space very slowly and to sample as many points in the space as possible on each iteration. The main limitation on T is the available computing power, and the value of R must be balanced with the value of I to control the width of the parameter space at the end of the fit.

If the parameter space has a width ΔX_0 along dimension X at the beginning of the fit, the final width in that dimension will be

$$\Delta X = (\Delta X_0) R^I. \tag{17}$$

This gives an estimate for the uncertainty of the fit result in each dimension. This final uncertainty can be reduced by either using a larger value of I or a smaller value of R. Additionally, if a good initial estimate of the parameters is known, the size of the initial parameter space can be made smaller, reducing the number of iterations needed to achieve the same level of convergence.

The values of the fit parameters were optimized by fitting one simulated event repeatedly with a number of sets of fit parameters. The results of these fits were then compared to the known correct answer and labeled as "correct" if they were within a tolerance of 10 mm in each dimension for the vertex position, 100 keV for the initial proton energy, 5° for the azimuthal angle, and 2° for the scattering angle. The proportion of correct results for each set of parameters was calculated, and these proportions are shown in Fig. 15. The results suggest that the Monte Carlo algorithm is most likely to converge to the correct minimum when T is large and R and I are chosen such that the parameter space is slowly compressed over many iterations.

The set of parameters used to fit the ^{46}Ar(p, p) data is listed in Table 1. Note that this is not the same set of parameters as the best one identified in Fig. 15. The parameters from Table 1 were chosen as a compromise between quality of fit and computation time; increasing the number of iterations from 20 to 30 to reach the best parameter set would increase computation time by 50 % for a relatively small gain in resolution. Any effect that the quality of fit has on the resolution is reflected in the simulated resolutions presented in Section 4.2 below.

4. Simulated performance

4.1. Track generation and fitting

To establish expectations for detector resolution in the commissioning experiment, the elastic scattering of a radioactive ^{46}Ar beam on protons from isobutane gas was simulated. The proton tracks were simulated using the same particle tracking code that was used in the Monte Carlo fitting procedure described above in Section 3.3. Using the same code for simulation and fitting helps to ensure that the simulated resolution is affected only by the modeled properties of the detector and the fitting procedure, and not by inconsistencies between the simulation and the fit.

Table 1
Monte Carlo fit parameters I, T, and R and initial parameter space widths σ used in the ^{46}Ar(p, p) measurement.

I	T	R	$\sigma_{x,y,z}$	σ_E	σ_ϕ	σ_θ
20	500	0.8	0.1 m	4.0 MeV	60°	30°

The simulated tracks were represented using the parameterization described above in Section 3.3. In this case, the values for x_0 and y_0 were chosen from a normal distribution with mean 0 mm and standard deviation 10 mm, and z_0 was varied uniformly between 0 m and 1 m. The azimuthal angle ϕ_0 was varied uniformly between 0 and 2π, and the polar angle θ_0 followed a uniform distribution between 10° and 90°. The vertex energy of the ^{46}Ar projectile was then calculated using the stopping power of the isobutane, and the energy E_0 of the proton was found as a function of the ^{46}Ar vertex energy and the scattering angle θ_0 using formulas from relativistic kinematics.

After tracking, the procedure described in Section 3.3 was used to simulate electron diffusion, project the simulated proton tracks onto the pad plane, and generate simulated GET electronics signals. Simulated noise and baseline offsets were added to these signals to more closely approximate real data. The simulated events were then reconstructed and analyzed using the procedure described in Section 3. A sample event and its fit are shown in Fig. 16.

4.2. Expected resolution

The procedure above was performed for 5.45×10^5 tracks and the result of the Monte Carlo fit for each track was compared to its known correct initial conditions to produce an estimate of the resolution expected from the AT-TPC. Gaussian fits to the distributions in Fig. 17 showed that the expected resolution in the energy of the scattered protons was 36.0 keV, and the scattering angle was found to a precision of 0.316°. These resolutions were calculated as the full width at half maximum (FWHM) of each distribution. The offset in Δz_0 is caused by the rise time of the simulated electronics signals which was not accounted for in this analysis. This does not affect experimental data since the experimental z calibration is done with respect to the peaks of the signals, thereby including this offset.

Using kinematics formulas, the ^{46}Ar vertex energy was reconstructed to a resolution of 84.1 keV/u. The vertex energy can also be deduced from the location of the vertex along the beam axis. This was done by comparing the initial position z_0 of the proton track to the location of the beam entrance window at $z = 1000$ mm. This difference is the distance traveled by the ^{46}Ar nucleus before it interacted with the scattered proton, which can be combined with energy loss data from SRIM to

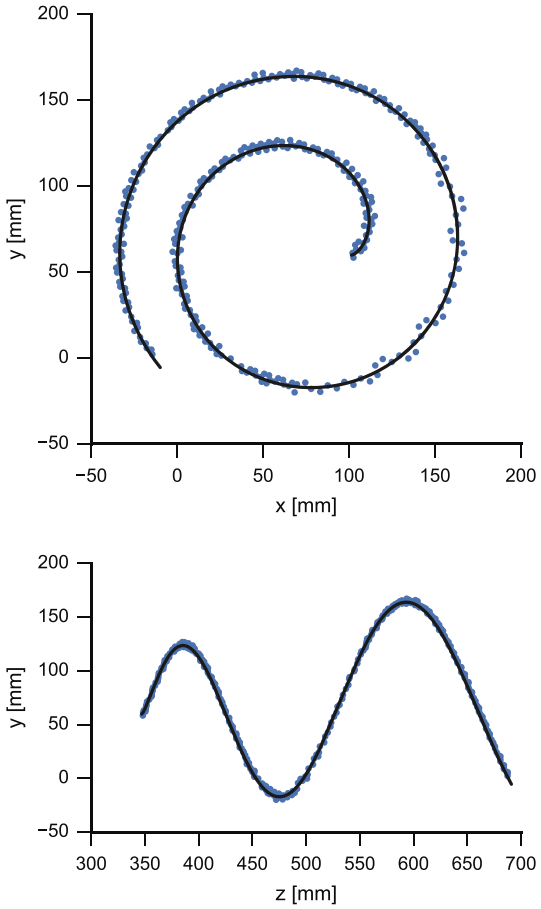

Fig. 16. A simulated proton track. The simulated data points are shown as blue dots, and the result of the Monte Carlo fit is shown as a black curve. The top plot shows the xy projection, which is like looking upstream from the anode end of the detector. The bottom plot shows the yz projection, which is like looking at the detector from the side. In the bottom plot, the proton starts on the right-hand side of the image and moves toward the left. The beam entrance window is located at $z = 1000$ mm on this axis, while the sensor plane is at $z = 0$ mm. This proton started with $E_0 = 1.85$ MeV moving at a scattering angle of $\theta_0 = 67.0°$. The Monte Carlo fit reconstructed the initial energy to within 8.14 keV and the scattering angle to within 0.0055°.

find the energy of the nucleus at the reaction site. The resolution of this positional vertex energy was 41.4 keV/u.

Fig. 18 shows the resolution achieved by the two vertex energy reconstructions along with the difference between the two. The ability to compare these two determinations is essential to separate elastic scattering from inelastic scattering, which would show up as a separate peak on the difference spectrum due to the different kinematics.

4.3. Simulated efficiency

The simulated events described above were also used to study the efficiency of the trigger setup used in the commissioning experiment. As described in Section 2.7, the AT-TPC was triggered using an ad hoc global multiplicity trigger generated by combining the 10 CoBo-level multiplicity trigger signals using a logical OR operation. This was modeled in software by generating a simulated AGET trigger signal for each channel that contained a square trigger pulse with width 235 ns and amplitude 48 ADC bins [14] whenever the signal in that channel was above threshold. These simulated trigger signals were summed and then convolved with a 12 μs multiplicity window to form simulated CoBo-level multiplicity signals. The simulated event was then considered to trigger the electronics if any of these simulated CoBo-level multiplicity signals rose above a threshold of 20 000.

Fig. 19 shows simulated efficiency curves calculated using this trigger simulation and the Monte Carlo fit. The acceptance of the trigger was somewhat limited, and most events at large center-of-mass scattering angles were rejected. Large angles in the center-of-mass frame correspond to very forward scattering angles in the laboratory frame, so the rejected events were projected onto a small number of pads on the sensor plane, producing relatively long signals in each one. Assuming a drift velocity of 5.2 cm/μs, the 12 μs multiplicity window used here covers only approximately 60 % of the length of the active volume. This implies that the events may have been rejected because they did not activate enough channels within the multiplicity window in any one CoBo to trigger it.

5. Commissioning with radioactive beam

The AT-TPC was commissioned with a reaccelerated 4.6 MeV/u beam of radioactive ^{46}Ar from the ReA3 facility at the NSCL. The detector was filled with isobutane at 19.2 torr to measure the same

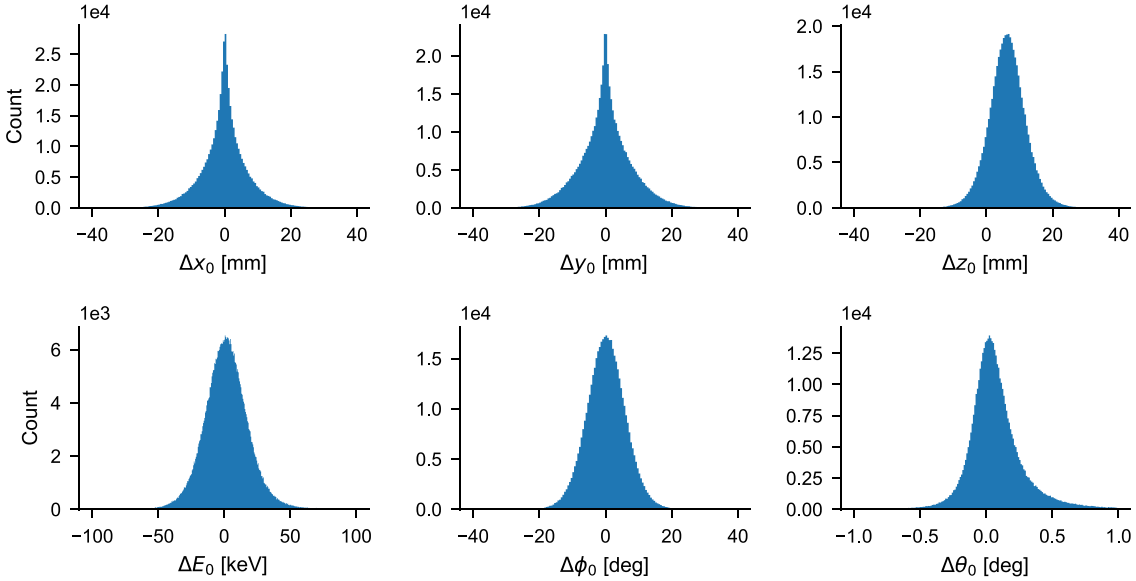

Fig. 17. The expected resolution of the AT-TPC for the reaction described in Section 4.1. The deviations between the reconstructed and true values are shown for the 6 fit parameters.

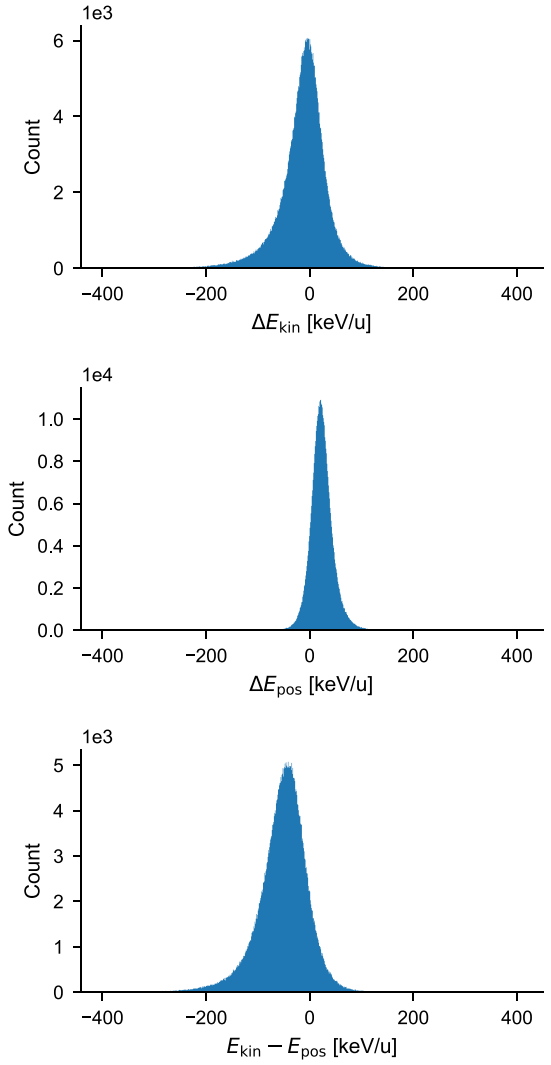

Fig. 18. Simulated resolution of ^{46}Ar vertex energies reconstructed by the two methods described in Section 4.2. The top plot shows the error in the vertex energy reconstructed from kinematics, ΔE_{kin}, defined as the energy value produced from the Monte Carlo fit minus the value calculated from the parameters input to the simulation. The middle plot shows a similar error calculated for the vertex energy as found from vertex position along the beam axis. The bottom plot shows the difference between the two reconstructions.

^{46}Ar(p, p) elastic scattering reaction as was simulated above. The detector parameters and electronics settings used in the experiment are given in Table 2. The average beam particle rate was 1180 Hz, although the instantaneous rate was much higher due to the beam structure discussed below. Over the course of 183.5 h of recording, 9.3 TB of data was produced, giving an average data rate of 14 MB/s or 1.2 TB/d.

One of the main challenges in using the AT-TPC for this type of reaction is the large dynamic range needed to detect the tracks of both the proton ($Z = 1$) and the ^{46}Ar nucleus ($Z = 18$) due to the large difference in energy loss between these two particles. Even though the electronics gain of the trigger exclusion region corresponding to the location of the ^{46}Ar beam tracks (similar to that shown in Fig. 12) was reduced to its minimum value, the electron amplification gain of the Micromegas needed to detect the proton track was too high in this region and caused a large saturation of the first stage of the electronics as well as noise on other channels due to cross-talk within adjacent channels of the electronics. Because of the gain reduction in the trigger exclusion region, the part of the proton track closest to the reaction vertex is missing and has to be extrapolated during the fitting procedure. In addition, the saturation of the electronics channels connected to the pads receiving the electrons from ^{46}Ar beam tracks distorted the signals enough to render the data all but useless; therefore, the track information from the beam was lost.

Table 2
Detector parameters used in the commissioning experiment.

Parameter	Value	Units
Electric field	9.5	kV/m
Magnetic field	1.68	T
Tilt angle	6.2	deg
Mesh potential	450	V
Last ring potential	500	V
Ion chamber potential	100	V
Gas pressure	19.2	torr
Clock frequency	12.5	MHz
Shaping time	280	ns
Channel threshold	100	ADC bins
Multiplicity threshold	20 000	–
Multiplicity window	12	μs
GET electronics gain	120	fC

Another factor that contributed to the degradation of the data is the pulsed nature of the ^{46}Ar beam due to its production mode in the Electron Beam Ion Source (EBIS). The extraction from such a source has a typical duty factor of less than 10 %, meaning that the beam particles arrive at the detector bunched together in a short time. Combined with the very high electron gain mentioned above, this caused large variations in the mesh current, leading to large fluctuations of the electron gain of the Micromegas. In addition, because all pads on the sensor plane are capacitively coupled through the Micromegas mesh, these fluctuations caused baseline shifts on individual channels that sometimes prevented these channels from triggering their discriminator and being recorded. This explains the gaps observed on many of the proton tracks recorded during this commissioning experiment. The low duty factor of the incoming beam also induced a large probability of pile-up (about 50 %) where more than one ^{46}Ar was present in the active volume of the detector within the time window of the data acquisition system (40 μs in this case). The pile-up events can be rejected easily using the ion chamber (see Section 2.6) located upstream of the detector.

After reconstruction and noise removal as described in Sections 3.1 and 3.2, the tracks were fitted using the same method as described above in Section 3.3. A cut was applied to the resulting χ^2 distributions to remove poorly fit tracks and separate proton tracks from tracks produced by scattering on a carbon nucleus from the isobutane molecule (see Fig. 20). This was possible due to the fact that the carbon nuclei, with their larger charge, deposit much more energy per unit track length into the gas than the protons. Additionally, the magnetic rigidity of a ^{12}C nucleus is twice that of a proton. These two effects cause the χ^2 value of the fit to a carbon track to be larger than for a proton track since the fitting algorithm assumes the track was produced by a proton.

Fig. 21 shows an example of an event that was fit well by the algorithm described above. The fitter was able to converge in spite of the small gaps in the track and the fact that the section of the track nearest to the beam was missing. These are both common features in the dataset, so it is important that the fitter can handle them.

Although some tracks like the one in Fig. 21 were fit well, the commissioning dataset has a number of properties that make it difficult to analyze and obtain the desired resolutions as calculated from the simulations. In particular, the absence of reliable data for the tracks of the incoming beam particles increases the error on the determination of the scattering angle of the scattered proton to a few degrees. This error then translates into an error in the kinematic vertex energy of about 0.5 MeV/u to 1.0 MeV/u, an order of magnitude larger than the expected resolution. As a result, the comparison between the reaction energies as determined from the location of the vertex and the kinematic properties of the scattered proton is poor.

To confirm that this uncertainty was the cause of the discrepancy between the two energy reconstructions in the experimental data, the

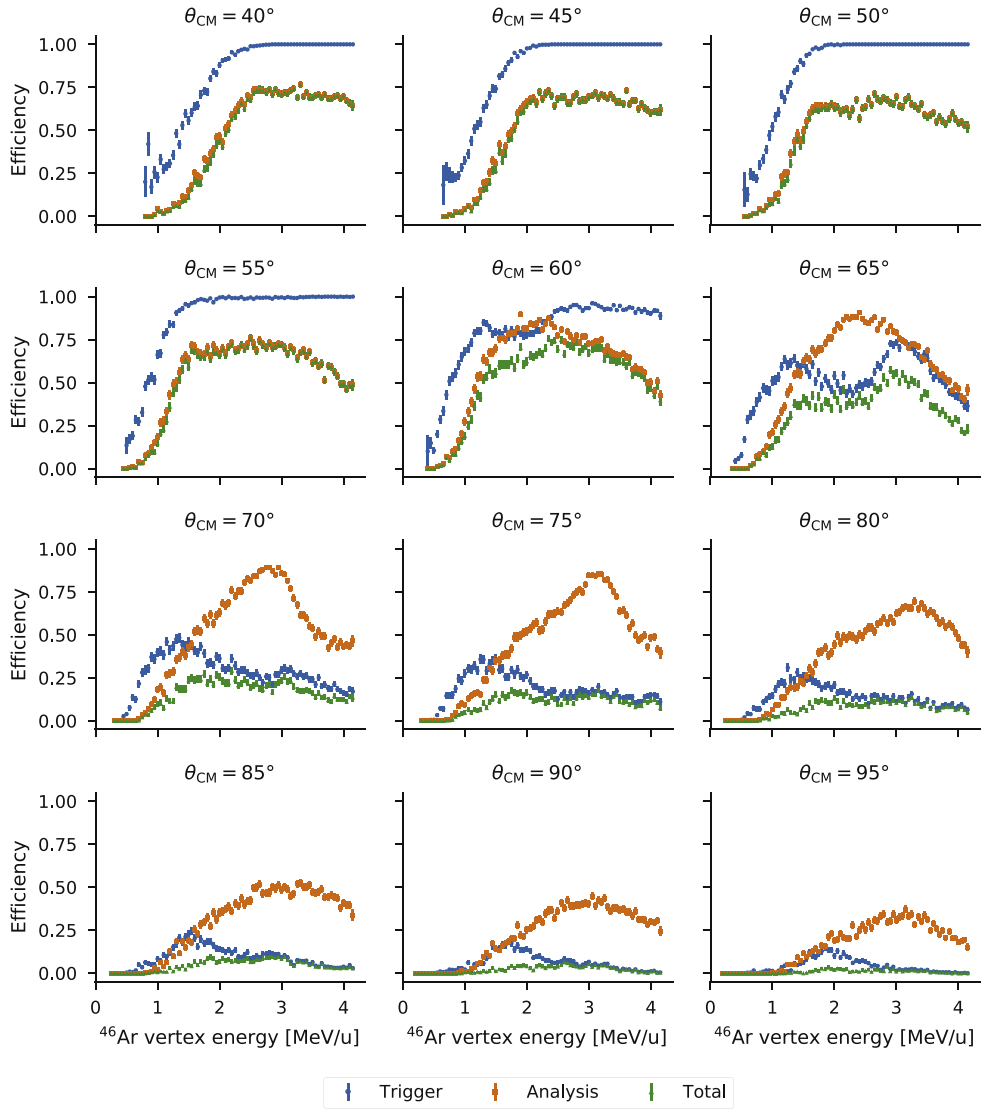

Fig. 19. Simulated efficiencies as a function of ^{46}Ar vertex energy at several scattering angles. The trigger and the Monte Carlo analysis both contribute to a loss of efficiency at large scattering angles, but the trigger has the dominant effect.

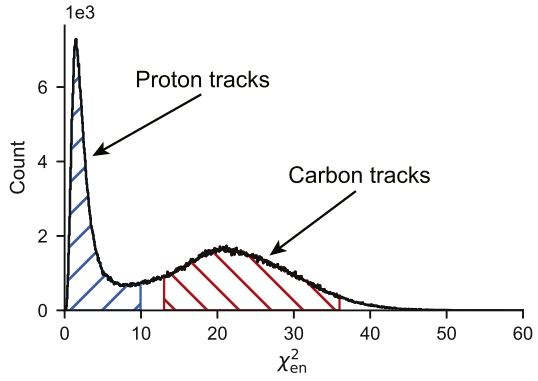

Fig. 20. Commissioning data distribution of χ^2_{en}, as defined in (14). The events in the left-hand peak were produced by scattered protons, whereas the tracks in the right-hand peak were produced primarily by scattering on carbon.

simulation of the experiment was modified to include protons produced by ^{46}Ar nuclei moving at an angle of up to 2° from the beam axis. This greatly decreased the accuracy of the kinematic vertex energy reconstruction, thereby increasing the difference between the two reconstructions to match the experimental data (see Fig. 22). It did not, however, significantly affect the accuracy of the positional vertex energy reconstruction.

For this particular dataset, the best reaction energy resolution is therefore achieved from the determination of the vertex location relative to the entrance window of the detector. Such a distribution is shown in Fig. 23, where the sharp edge close to $z = 1000$ corresponds to the location of the entrance window. A fit to this edge using a modified Gaussian cumulative distribution function gives an estimated resolution of 46.4 keV/u for the reaction energy.

6. Conclusion

The AT-TPC, a time projection chamber with an active target, has been designed, built, and commissioned at the NSCL. The active-target design gives the detector a high efficiency essential in experiments with low incident beam energies and low counting rates. The AT-TPC is mounted inside a 2 T solenoidal magnetic field that curves the trajectories of charged particles to increase their track length in the detector and provide more information about their energy via magnetic rigidity.

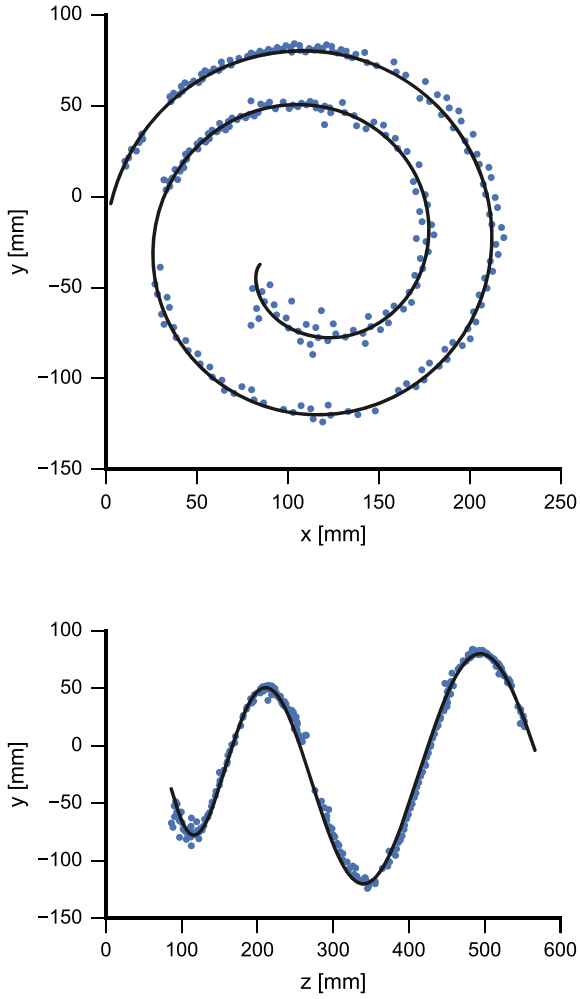

Fig. 21. A sample event from the commissioning run with ^{46}Ar. This event was found to have a proton energy of 2.081 MeV and a scattering angle of 63.5°, both in the laboratory frame. The energy of the ^{46}Ar nucleus at the vertex was reconstructed as 2.73 MeV/u. The kinematic and positional reconstructions agreed to within 9 keV/u for this particular event.

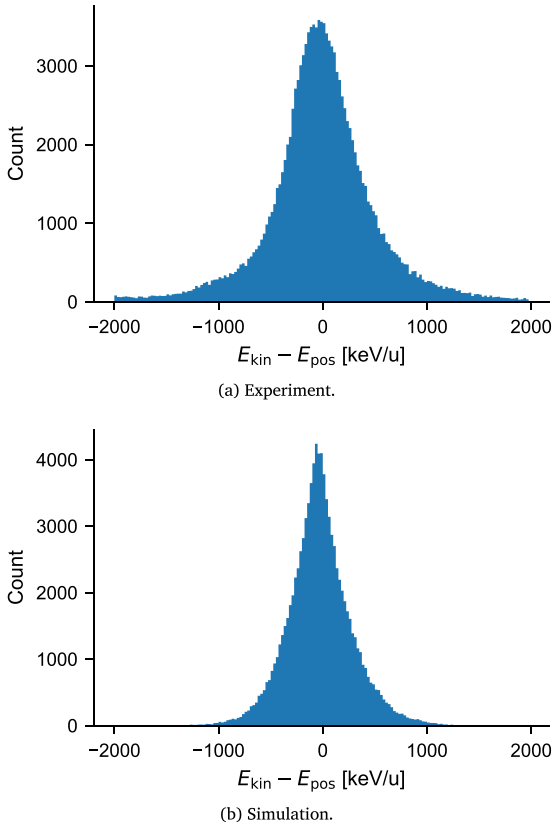

(a) Experiment.

(b) Simulation.

Fig. 22. Difference between the ^{46}Ar vertex energy as reconstructed from kinematics and vertex position in (a) the experiment and (b) a simulation including the emittance of the beam. The uncertainty introduced by the varying orientation of the beam track decreases the accuracy of the energy reconstruction from kinematics, increasing the difference between the two reconstructions as compared to the result from Fig. 18, where this effect was not included.

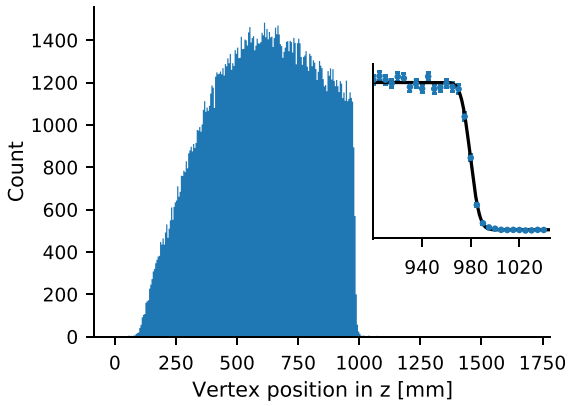

Fig. 23. Vertex position distribution from the commissioning data. Each vertex location is deduced from an extrapolation of the proton track to the beam axis after fitting by the Monte Carlo algorithm. The sharp edge close to $z = 1000$ mm corresponds to the location of the entrance window. The z position resolution calculated from fitting this edge is 14.1 mm FWHM, which corresponds to the energy resolution of 46.4 keV/u quoted in the text.

The AT-TPC is instrumented with the GET electronics, a flexible, distributed, digital data acquisition system designed to address the needs of TPCs. This system can accept the high data flow from the detector while providing the flexibility to use different configurations and trigger setups in different experiments. In particular, the ability to self-trigger the detector based on hit multiplicity combined with exclusion regions is essential to avoid recording unnecessary events and to lower the dead time of the acquisition system.

Although the tracks recorded in the AT-TPC cannot be described by an analytic function, they are easily fit using a simulation-based Monte Carlo optimization algorithm. While somewhat costly in computational resources, this method is able to reconstruct simulated proton tracks to resolutions of 36.0 keV FWHM for the energy and 0.32° FWHM for the scattering angle. The simulations also demonstrate the capability to determine the reaction energy from both the vertex location and the kinematics of the scattered particle consistently to within 100 keV/u. This ability is essential to separate elastic and inelastic components of the reactions studied in this device.

The AT-TPC was commissioned using a beam of radioactive ^{46}Ar at 4.6 MeV/u to perform resonant proton scattering. Several issues hindered the quality of the data, which resulted in poorer resolution than expected for the reaction energy determined from the kinematic properties of the scattered protons. However, the resolution obtained from the determination of the vertex position remains acceptable for the experimental goals at 46.4 keV/u.

The electronics saturation issues encountered during the commissioning run are being addressed by individually polarizing the pads. This method was previously applied to the Prototype AT-TPC in an experiment using reactions between a ^{10}Be beam and ^{4}He target [5]. Using

this method, the electron gain of the Micromegas can be reduced by several orders of magnitude for only the pads corresponding to the beam tracks. This prevents not only the saturation of the electronics, but also the large mesh current fluctuations observed during the commissioning experiment that compromised the quality of the data. A prototype of the interface board placed between the pad plane and the GET front-end electronics enabling the individual polarization of pads is currently being tested.

The limited trigger acceptance seen in the commissioning experiment will be avoided in the future by using the trigger simulations that are now available to simulate different sets of trigger parameters before the experiment. Additionally, the true global multiplicity trigger provided by the MuTAnT board should prevent events from being rejected if they activate only a few pads in each CoBo.

Finally, the statistics of future proton scattering experiments will be greatly improved by filling the active volume with pure hydrogen gas instead of isobutane. This eliminates the unwanted carbon scattering events and increases the density of proton scattering centers by a factor of 5 compared to the same amount of isobutane gas. This will be made possible by installing a multi-layer thick GEM device [22] in front of the Micromegas to provide additional electron amplification.

Acknowledgments

The Micromegas device used in the AT-TPC was fabricated by S. Aune at the Saclay IRFU MPGD Workshop. Computational resources for this work were provided by the Institute for Cyber-Enabled Research at Michigan State University. Construction of the AT-TPC was partially supported by the National Science Foundation (NSF) under grant no. MRI-0923087. The commissioning of the AT-TPC was supported by the NSF under cooperative agreement no. PHY-1102511.

References

[1] A.C.C. Villari, D. Alt, G. Bollen, D.B. Crisp, M. Ikegami, S.W. Krause, A. Lapierre, S.M. Lidia, D.J. Morrissey, S. Nash, R.J. Rencsok, R. Ringle, S. Schwarz, R. Shane, C. Sumithrarachchi, S.J. Williams, Q. Zhao, Commissioning and First Accelerated Beams in the Reaccelerator (ReA3) of the National Superconducting Cyclotron Laboratory, MSU, in: Proceedings of IPAC2016, 2016, pp. 4–7. http://dx.doi.org/10.18429/JACoW-IPAC2016-TUPMR024.

[2] S. Beceiro Novo, T. Ahn, D. Bazin, W. Mittig, Active targets for the study of nuclei far from stability, Prog. Part. Nucl. Phys. 84 (2015) 124–165. http://dx.doi.org/10.1016/j.ppnp.2015.06.003.

[3] D. Suzuki, M. Ford, D. Bazin, W. Mittig, W. Lynch, T. Ahn, S. Aune, E. Galyaev, A. Fritsch, J. Gilbert, F. Montes, A. Shore, J. Yurkon, J. Kolata, J. Browne, A. Howard, A. Roberts, X. Tang, Prototype AT-TPC: Toward a new generation active target time projection chamber for radioactive beam experiments, Nucl. Instrum. Methods Phys. Res. Sect. A 691 (2012) 39–54. http://dx.doi.org/10.1016/j.nima.2012.06.050.

[4] D. Suzuki, A. Shore, W. Mittig, J.J. Kolata, D. Bazin, M. Ford, T. Ahn, F.D. Becchetti, S. Beceiro Novo, D. Ben Ali, B. Bucher, J. Browne, X. Fang, M. Febbraro, A. Fritsch, E. Galyaev, A.M. Howard, N. Keeley, W.G. Lynch, M. Ojaruega, A.L. Roberts, X.D. Tang, Resonant α scattering of ^{6}He: Limits of clustering in ^{10}Be, Phys. Rev. C 87 (5) (2013) 1–14. http://dx.doi.org/10.1103/PhysRevC.87.054301.

[5] A. Fritsch, S. Beceiro Novo, D. Suzuki, W. Mittig, J.J. Kolata, T. Ahn, D. Bazin, F.D. Becchetti, B. Bucher, Z. Chajecki, X. Fang, M. Febbraro, A.M. Howard, Y. Kanada-En'yo, W.G. Lynch, A.J. Mitchell, M. Ojaruega, A.M. Rogers, A. Shore, T. Suhara, X.D. Tang, R. Torres-Isea, H. Wang, One-dimensionality in atomic nuclei: A candidate for linear-chain α clustering in ^{14}C, Phys. Rev. C 93 (2016) 014321. http://dx.doi.org/10.1103/PhysRevC.93.014321.

[6] J.J. Kolata, A.M. Howard, W. Mittig, T. Ahn, D. Bazin, F.D. Becchetti, S. Beceiro Novo, Z. Chajecki, M. Febbrarro, A. Fritsch, W.G. Lynch, A. Roberts, A. Shore, R.O. Torres-Isea, Fusion studies with low-intensity radioactive ion beams using an active-target time projection chamber, Nucl. Instrum. Methods Phys. Res. Sect. A 830 (2016) 82–87. http://dx.doi.org/10.1016/j.nima.2016.05.036.

[7] Y. Ayyad, M. Cortesi, W. Mittig, D. Bazin, CO_2 operation of an active target detector readout based on THGEM, J. Instrum. 12 (06) (2017) P06003. http://dx.doi.org/10.1088/1748-0221/12/06/P06003.

[8] R.S. Henderson, Y.I. Davydov, W. Faszer, D.D. Koetke, L.V. Miasoedov, R. Openshaw, M.A. Quraan, J. Schaapman, V. Selivanov, G. Sheffer, T.D.S. Stanislaus, V. Torokhov, Precision planar drift chambers and cradle for the TWIST muon decay spectrometer, Nucl. Instrum. Methods Phys. Res., Sect. A 548 (3) (2005) 306–335. http://dx.doi.org/10.1016/j.nima.2005.02.043.

[9] R. Veenhof, Garfield, recent developments, Nucl. Instrum. Methods Phys. Res. Sect. A 419 (2–3) (1998) 726–730. http://dx.doi.org/10.1016/S0168-9002(98)00851-1.

[10] I. Giomataris, R. De Oliveira, S. Andriamonje, S. Aune, G. Charpak, P. Colas, G. Fanourakis, E. Ferrer, A. Giganon, P. Rebourgeard, P. Salin, Micromegas in a bulk, Nucl. Instrum. Methods Phys. Res. Sect. A 560 (2) (2006) 405–408. http://dx.doi.org/10.1016/j.nima.2005.12.222.

[11] Y. Giomataris, P. Rebourgeard, J. Robert, G. Charpak, MICROMEGAS: a high-granularity position-sensitive gaseous detector for high particle-flux environments, Nucl. Instrum. Methods Phys. Res. Sect. A 376 (1) (1996) 29–35. http://dx.doi.org/10.1016/0168-9002(96)00175-1.

[12] E. Pollacco, S. Anvar, H. Baba, P. Baron, D. Bazin, C. Belkhiria, B. Blank, J. Chavas, P. Chomaz, E. Delagnes, F. Druillole, P. Hellmuth, C. Huss, E. Galyaev, B. Lynch, W. Mittig, T. Murakami, L. Nalpas, J.-L. Pedroza, R. Raabe, J. Pibernat, B. Raine, A. Rebii, A. Taketani, F. Saillant, D. Suzuki, N. Usher, G. Wittwer, GET: A generic electronic system for TPCs for nuclear physics experiments, Phys. Proc. 37 (2012) 1799–1804. http://dx.doi.org/10.1016/j.phpro.2012.02.506.

[13] S. Anvar, P. Baron, B. Blank, J. Chavas, E. Delagnes, F. Druillole, P. Hellmuth, L. Nalpas, J.L. Pedroza, J. Pibernat, E. Pollacco, A. Rebii, N. Usher, AGET, the GET front-end ASIC, for the readout of the time projection chambers used in nuclear physic experiments, IEEE Nucl. Sci. Symp. Conf. Record (2012) 745–749. http://dx.doi.org/10.1109/NSSMIC.2011.6154095.

[14] P. Baron, E. Delagnes, AGET, a Front End ASIC for Active Time Projection Chamber: Data Sheet, 2013.

[15] T. Lohse, W. Witzeling, The time projection chamber, in: F. Sauli (Ed.), Instrumentation in High Energy Physics, World Scientific, Singapore, 1992, pp. 82–156.

[16] Y. Ayyad, W. Mittig, D. Bazin, M. Cortesi, Overview of the data analysis and new micro-pattern gas detector development for the active target time projection chamber (AT-TPC) project, J. Phys. Conf. Ser. 876 (1) (2017) 012003. http://dx.doi.org/10.1088/1742-6596/876/1/012003.

[17] Y. Ayyad, Forthcoming publication on analysis methods for the AT-TPC, Nucl. Instrum. Methods Phys. Res. Sect. A.

[18] R.O. Duda, P.E. Hart, Use of the Hough transformation to detect lines and curves in pictures., Comm. ACM 15 (1) (1972). http://dx.doi.org/10.1145/361237.361242.

[19] J. Illingworth, J. Kittler, The adaptive hough transform, IEEE Trans. Pattern Anal. Mach. Intell. PAMI-9 (5) (1987) 690–698. http://dx.doi.org/10.1109/TPAMI.1987.4767964.

[20] I. Heinze, Development of a Hough Transformation Track Finder for Time Projection Chambers, University of Hamburg, 2013.

[21] J.F. Ziegler, M.D. Ziegler, J.P. Biersack, SRIM - The stopping and range of ions in matter (2010), Nucl. Instrum. Methods Phys. Res. Sect. B 268 (11–12) (2010) 1818–1823. http://dx.doi.org/10.1016/j.nimb.2010.02.091.

[22] M. Cortesi, S. Rost, W. Mittig, Y. Ayyad-Limonge, D. Bazin, J. Yurkon, A. Stolz, Multi-layer thick gas electron multiplier (M-THGEM): A new MPGD structure for high-gain operation at low-pressure, Rev. Sci. Instrum. 88 (1) (2017) 013303. http://dx.doi.org/10.1063/1.4974333.